Pergamon

Int. J. Heat Mass Transfer. Vol. 39, No. 14, pp. 2925–2935, 1996

0017-9310/96 $15.00 + 0.00

0017-9310(95)00381-9

Heat transfer on the base surface of three-dimensional protruding elements

M. K. CHYU and V. NATARAJAN

Department of Mechanical Engineering, Carnegie Mellon University, Pittsburgh, PA 15213, U.S.A.

(*Received* 29 *July* 1994 *and in final form* 10 *October* 1995)

Abstract—Five basic geometries (cylinder, cube, diamond, pyramid and hemisphere) are comparatively examined at a Reynolds number of 1.7×10^4 to determine the effect of a single roughness element on surface heat (mass) transfer. Local mass transfer measurements obtained using the naphthalene sublimation technique are substantiated by flow visualization. Results show that the upstream horseshoe vortex system and the inverted arch-shaped vortex immediately behind the elements are the dominating effects in element–endwall interaction. Based on information concerning the extent of spanwise influence of each element, an inter-element spacing may be proposed for array configurations to achieve optimal heat transfer performance. Copyright © 1996 Elsevier Science Ltd.

INTRODUCTION

Thermal control using heat transfer enhancement in modern applications, such as heat exchangers, electronic devices, propulsion and power systems, etc. requires a basic understanding of convective transport around three-dimensional elements. Compared to its two-dimensional counterpart, such as transverse-ribs mounted on a channel wall, a three-dimensional element is so named because it induces a three-dimensional flowfield around the element. To date, information concerning three-dimensional roughness heat transfer has relied primarily on area-averaged measurements, which typically involve arrays of roughness elements [1]. While such information is indeed useful for traditional heat exchanger design calculations, it is grossly insufficient in discerning local transport phenomena induced by the element. To achieve significant advancements in the design of optimal heat transfer surfaces, it is crucial to understand the local nature of the surface heat transfer. Currently, this is an issue of increasing importance, particularly for applications that require critical cooling strategies, such as those mentioned earlier. Bearing these concerns in mind, the present study examines local heat transfer characteristics in the vicinity of individual protruding elements. Specifically, the tasks performed here are designed to compare the effects of five fundamental three-dimensional geometries on the wall heat transfer. The five elements are: (1) cylinder, (2) cube, (3) diamond, (4) pyramid and (5) hemisphere. Knowledge gained from this study may provide thermal designers with guidelines for array arrangement involving multiple elements.

Much of the earlier research concerning heat transfer of three-dimensional, wall-mounted protrusions has focused primarily on the short cylinder. This is attributable to both the wide application and the associated fundamental importance of the cylindrical geometry. Using a heat and mass transfer analogy, Goldstein *et al.* investigated the heat transfer distributions on an endwall mounted with a short cylinder [2] and cylinder arrays [3]. They have reported two main features that dominate the transport process in the system: (1) horseshoe vortices due to protrusion–endwall interaction and (2) downstream reattachment due to shear layer separation. While the horseshoe–vortex structure prevails virtually for any three-dimensional bluff body near the endwall junction, the second feature is rather insignificant for tall obstacles. Fisher and Eibeck [4], using the liquid crystal technique, measured the local heat transfer in the wake region for both circular and tapered cylinders.

Apart from the cylinder, the cubical element appears to be the second most investigated geometry in the open literature. The majority of non-cylinder related studies are motivated by their relevance to environmental aerodynamics and wind loading on building structures. Hence, only the momentum transfer around an obstacle embedded in a thick boundary layer is emphasized. Virtually all the previous studies reveal that flow in the cube vicinity is highly three-dimensional and dominated by a number of vortices far more complex than those around a cylinder [5–7]. Such a flowfield has recently been modeled numerically using the large-eddy turbulence simulation [8]. Also, to simulate forced convective cooling of electronic packages, heat transfer from the surface of a wall-mounted cube has attracted significant attention recently [9–11]. However, no work has been reported on the heat transfer from the endwall. There have been very few studies on geometries other than the cylinder or the cube. Ogawa *et al.* [12] investigated the flowfield of diamond-shaped obstacle by positioning

NOMENCLATURE

D	obstacle height
dy	change in depth of mass transfer surface
dt	run time of experiment
h	heat transfer coefficient, equation (1)
h_m	naphthalene mass transfer coefficient, equation (2)
m	mass transfer flux of naphthalene from surface
k	thermal conductivity
Pr	Prandtl number, ν/α
q	heat flux from wall
Re	Reynolds number, UD/ν
Sc	naphthalene–air Schmidt number, ν/Γ
St	naphthalene mass transfer Stanton number, h_m/U
St_0	flat plate mass transfer Stanton number
$(St/St_0)_m$	mass transfer enhancement averaged over domain of influence
(St_m/St_0)	maximum enhancement downstream of protrusion
T_w	temperature of wall
T_∞	temperature of freestream
t	time
U	velocity of free stream
X, Z	coordinate system as shown in Fig. 1
X_F	primary separation point upstream of protrusion
X_R	location of flow reattachment behind protrusion
Z_S	domain of spanwise influence.

Greek symbols

α	thermal diffusivity of air
Γ	naphthalene–air diffusion coefficient
ν	kinematic viscosity of air
$\rho_{v,w}$	vapor mass concentration or density of naphthalene at the wall
ρ_∞	vapor mass concentration or density of naphthalene in freestream, zero in the present study
ρ_S	density of solid naphthalene
Δ	finite difference operator.

a cube at 45° to the mainstream direction. Using the hot-wire anemometry and flow visualization in a water tunnel, Savory *et al.* [13, 14] have examined the flow features in the near-wake region of a hemisphere.

Within the context of heat transfer enhancement, Mantle [15] investigated the endwall flow patterns for three different element geometries, i.e. cylinder, cube and diamond, using wool tufts and smoke tracers in a turbulent boundary layer. With an identical characteristic dimension at 1 in for all three individual elements, the range of maximum spanwise disturbance is 1.0, 1.3 and 2.7 in, respectively. Also, the location of reattachment is 1.75, 2.0 and 3.0 in respectively, downstream to the obstacle. Based on the idea that the flow disturbance must pervade the entire heat transfer surface, the study proposed and demonstrated that a heat transfer surface with a three-dimensional roughness array should have an inter-element spacing nearly twice the lateral spread.

To facilitate a comparative study, it is necessary to determine the detailed local heat transfer from the endwall caused by each one of the five protruding elements. Considerable difficulties may be encountered in the measurement of local heat transfer or temperature using conventional thermal methods due to unavoidable heat loss and insulation among a large number of sensors. Alternatively, the present study uses a mass transfer analogous system based on naphthalene ($C_{10}H_8$) sublimation. By invoking an analogy between heat and mass transfer, results obtained from the mass transfer measurement can be transformed into their heat transfer counterparts [16]. To enhance the data spatial-resolution as well as acquisition rate, the local mass transfer coefficient is determined using an automated, computer-controlled surface profile measurement system similar to that developed earlier by Goldstein *et al.* [2]. In an attempt to isolate the geometric effect, the present experiment is designed to simulate an element that is exposed to an external flow with a nearly zero-pressure gradient in the freestream.

PRINCIPLE OF HEAT AND MASS TRANSFER ANALOGY

The respective driving potentials for heat and mass transfer; i.e. $(T_w - T_\infty)$ and $(\rho_{v,w} - \rho_\infty)$, are equivalent from the standpoint of scalar transport between wall and freestream. Such an analogy also prevails for the transport coefficients, i.e.

$$h = q/(T_w - T_\infty) \tag{1}$$

$$h_m = m/(\rho_{v,w} - \rho_\infty). \tag{2}$$

Based on the fact that the naphthalene vapor concentration in the freestream is zero for the present external-flow system, equation (2) simplifies to

$$h_m = m\,dt/\rho_{v,w}. \tag{3}$$

Because the entire experimental system is maintained virtually isothermal, the naphthalene vapor concentration at the wall is constant. Hence the present mass transfer system is equivalent to a heat transfer study with constant wall temperature. The value of $\rho_{v,w}$ is evaluated using an ideal gas law in con-

junction with the wall temperature measured and a correlation between temperature and naphthalene vapor pressure proposed by Ambrose *et al.* [17].

The local mass transfer rate on a naphthalene surface depends on the change in surface thickness due to sublimation; i.e.,

$$dy = m\,dt/\rho_S \tag{4}$$

where ρ_S is the density of solid naphthalene. Combining equations (3) and (4) and integrating over the test duration yields the local mass transfer coefficient,

$$h_m = (\rho_S \Delta y)/(\rho_{v,w} \Delta t) \tag{5}$$

Its dimensionless counterpart, the Stanton number, is given as

$$St = h_m/U \tag{6}$$

where U is the freestream velocity.

EXPERIMENTAL SETUP AND PROCEDURE

The experiment uses an open circuit, suction-type wind tunnel with a 1.2 m long and 0.31 m square test section. The test section is preceded by a 16:1 contraction nozzle and four screens for inlet flow conditioning. Downstream of the test section, the tunnel exhaust is discharged out of the laboratory building to ensure that the inlet air is free of naphthalene. The test section of the wind tunnel is fitted with a plexiglas window for flow visualization, which substantiates the mass transfer results. As shown in Fig. 1, all roughness elements have a uniform characteristic dimension of 12.7 mm in height, width and diameter. Note that the "height" of the hemisphere is one-half the diameter. Also illustrated in the figure is the coordinate system designated for results presentation. As mentioned earlier, because the main objective here is to access the comparative effect among the individual elements, all tests are performed under the same Reynolds number at 1.7×10^4. This translates to a freestream velocity of approximately 20 m s^{-1}. The boundary layer near the location of the element (with the element absent), as measured by a pitot tube, exhibits a nearly 1/7th power-law correlation with a thickness approximately 2.5 times the element's characteristic size. The thickness of the viscous sublayer estimated at $y^+ = 5$ is about 0.08 mm. Turbulent intensity in the freestream, measured by a hot-wire anemometer, is less than 3%.

Prior to an actual run, both the endwall test plate and roughness element need to be coated with naphthalene. Coating of the element is done by dipping the element into a molten naphthalene pool for approximately one second, whereby a very thin naphthalene layer, approximately 1 mm in thickness, is solidified on the surface afterward. Since detailed mass transfer distribution over the element surface is not the main focus of this research, the local mass transfer measurement is performed on the endwall only. However, the overall amount of mass transfer from the entire element is determined by weighing the specimen before and after a test run. Such an average measurement uses a high precision electronic balance capable of resolving up to 0.003 mg.

Preparation of the endwall mass transfer region is enabled by casting molten naphthalene onto a 1.6 mm recess on a test plate made of aluminum. The surface cast, along with the naphthalene coated protruding element, is subsequently placed in the laboratory for at least a period of 8 h to gain a thermal equilibrium with the test room. To initiate an experiment, the test surface profile is measured first using a computer-controlled, data acquisition system, as mentioned earlier. The system comprises of a measurement table, stepper motors and controller, LVDT probe with transducer, digital voltmeter, and a personal computer. It takes about 2 s to complete a measurement cycle of each of data point on the test surface. The number of measurement points are 47×41 in the domain covering a rectangular region $-1.4 \leqslant x/D \leqslant 3.2$ and $-2.0 \leqslant z/D \leqslant 2.0$. This corresponds to a uniform step size of 1.27 mm in both x and z directions. Such an arrangement, in essence, amounts to using a total of 1927 discrete heat flux gauges over the measurement domain. The high spatial-resolution marks one of the most distinct advantages in employing the analogous mass transfer system for local heat transfer study. By geometry, data acquired over the present measurement domain are expected to be symmetric with respect to $z/D = 0$. Confirmation of this feature verifies the overall quality of the experiment.

On completion of the profile measurement, the naphthalene-coated element is screw-mounted onto the test plate and the assembly is then mounted onto the wind tunnel. It is exposed to the airstream for about 30 min, during which the temperature is monitored every 3 min using a precision thermistor. After the period of exposure, the element is removed and the surface profile is measured again. The change in depth due to sublimation during the period of wind exposure is used to evaluate the time-averaged mass transfer coefficients via the data reduction procedure described earlier. The total change in depth for each data point is on the order of 0.1 mm. For flow visualization, the oil–graphite streaklines on the endwall are photographed at the same flow condition as that of the mass transfer experiments.

RESULTS AND DISCUSSION

To provide a rational measure of the element-induced enhancement, the local mass transfer (Stanton number) is normalized by its flat plate counterpart; i.e. St/St_0. One key advantage of ratioing these two Stanton numbers is that the dependence of Prandtl number or Schmidt number may be eliminated, and the ratio can be directly applicable to the heat transfer situation. Local distribution of St_0 vs the streamwise coordinate, x, is measured prior to the

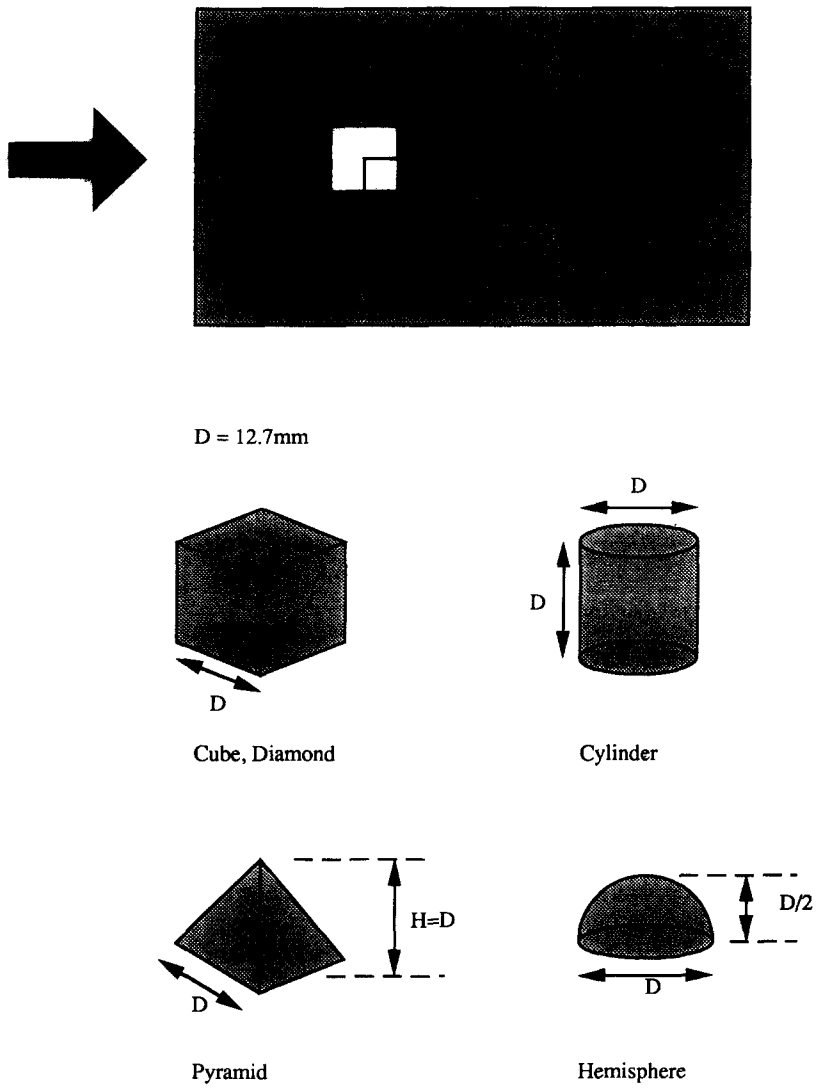

Fig. 1. Coordinate system and protrusion geometries.

actual experiments with obstacles. Figure 2 shows the data of St_0 obtained, which agree very favourably with the corresponding heat transfer values for turbulent flow over a flat plate with an unheated starting length

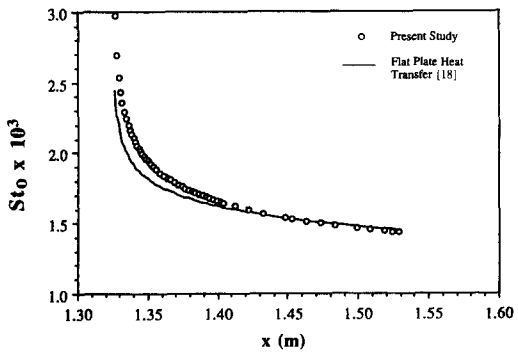

Fig. 2. Local heat transfer from a smooth flat surface.

[18]. This validates the reliability and accuracy of the present mass transfer system and analogy.

The local mass transfer results and the visualized flow patterns are presented in Figs 3 and 4. Both figures are comprised of five sub-figures (a)–(e), respectively, for each element. Figure 3 shows the contour plots for the mass transfer distribution over the entire measurement domain, whereas Fig. 4 displays the photos of oil streakline patterns on the endwall, which substantiates the mass transfer results. To facilitate a viable comparison, the extent of the domain of influence is defined as the furthest boundary where the presence of the obstacle has created at least a 25% heat transfer enhancement, i.e. $St/St_0 = 1.25$. A glance at both figures reveals excellent spanwise symmetry.

Cylinder

According to Fig. 3(a), local St/St_0 contours on the cylinder-mounted endwall displays a rather complex

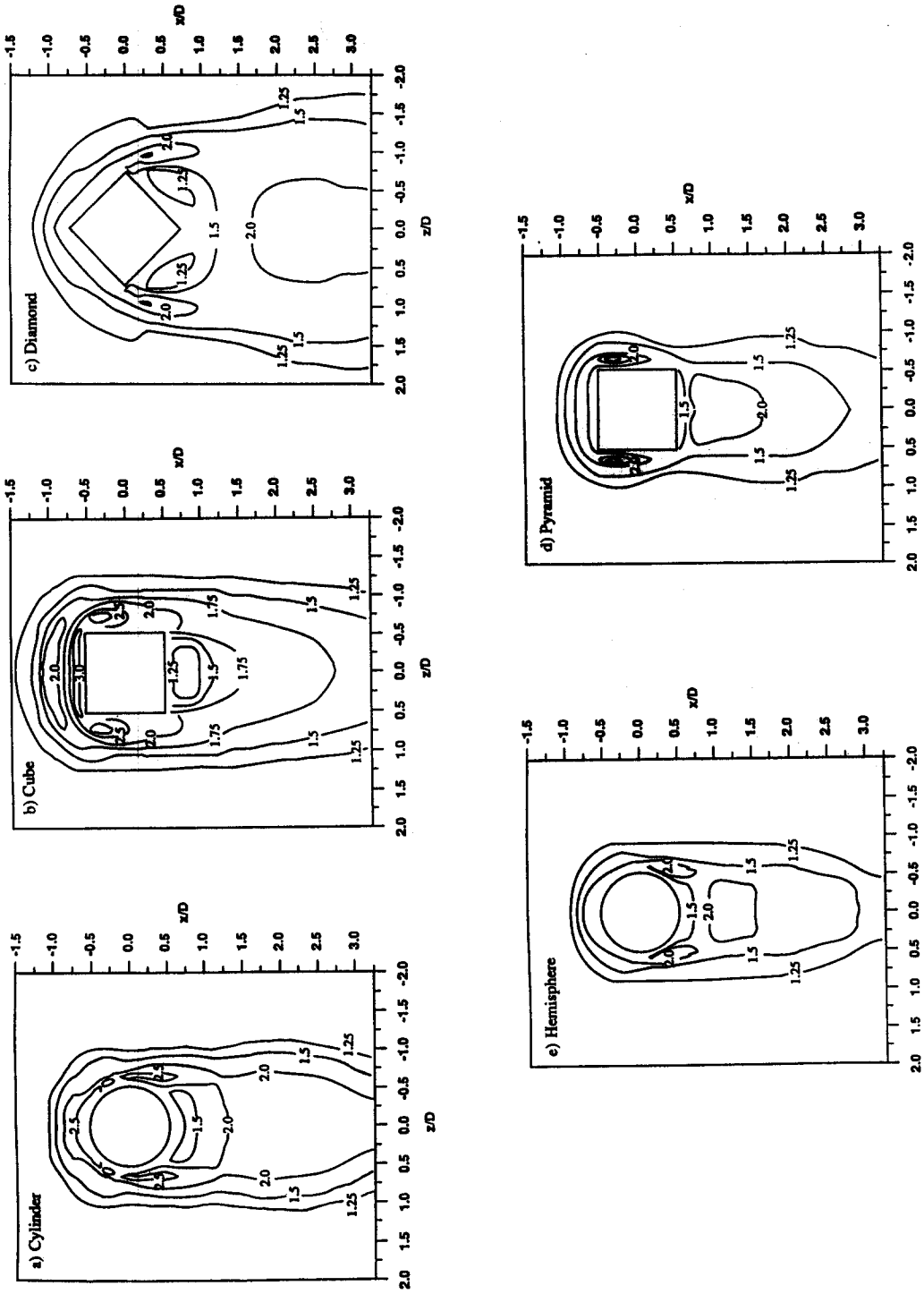

Fig. 3. St/St_0 contours on endwall mounted with an element: (a) cylinder; (b) cube; (c) diamond; (d) pyramid and (e) hemisphere.

Fig. 4. Oil–graphite streakline patterns near endwall: (a) cylinder; (b) cube; (c) diamond; (d) pyramid and (e) hemisphere. (*Continued opposite and overleaf.*)

pattern. Upstream of the cylinder, the effect of the protrusion extends to as much as one cylinder height, with St/St_0 close to unity. Proceeding downstream from here, the mass transfer gradually rises to reach a maximum, i.e. $St/St_0 \approx 2.5$, near the base–endwall junction. Such a high value is also present on either side of the cylinder, seen as elliptical contours. Immediately behind the cylinder, mass transfer is generally low. However, further downstream it increases monotonically to reach a local maximum, $St/St_0 \approx 2.2$ [not shown explicitly in Fig. 3(a)], at $x/D \approx 1.9$ along the center line. This maximum is attributable to the reattachment of the shear layer separated from the cylinder's top surface. After this point, the mass transfer declines due to the diminishing influence of the obstacle. The extent of the domain of influence, based on the boundary of 25% enhancement, is approximately $|Z_S/D| \approx 1.0$.

General trends of the mass transfer around the cylinder show a strong similarity to that reported earlier by Goldstein *et al.* [2]. However, actual values of St/St_0 for the present case are relatively lower, especially in the near-wake region of the cylinder. Among many possible factors, the differences in conditions of the approaching boundary layer may be the most significant. Although the magnitudes of Reynolds number are close and the near-wall velocity profiles are similar, the present boundary layer thickness relative to the cylinder height (or diameter) is about twice as much as the corresponding value in their study. From the standpoint of roughness effect, the level of disturbance by a given protrusion height is

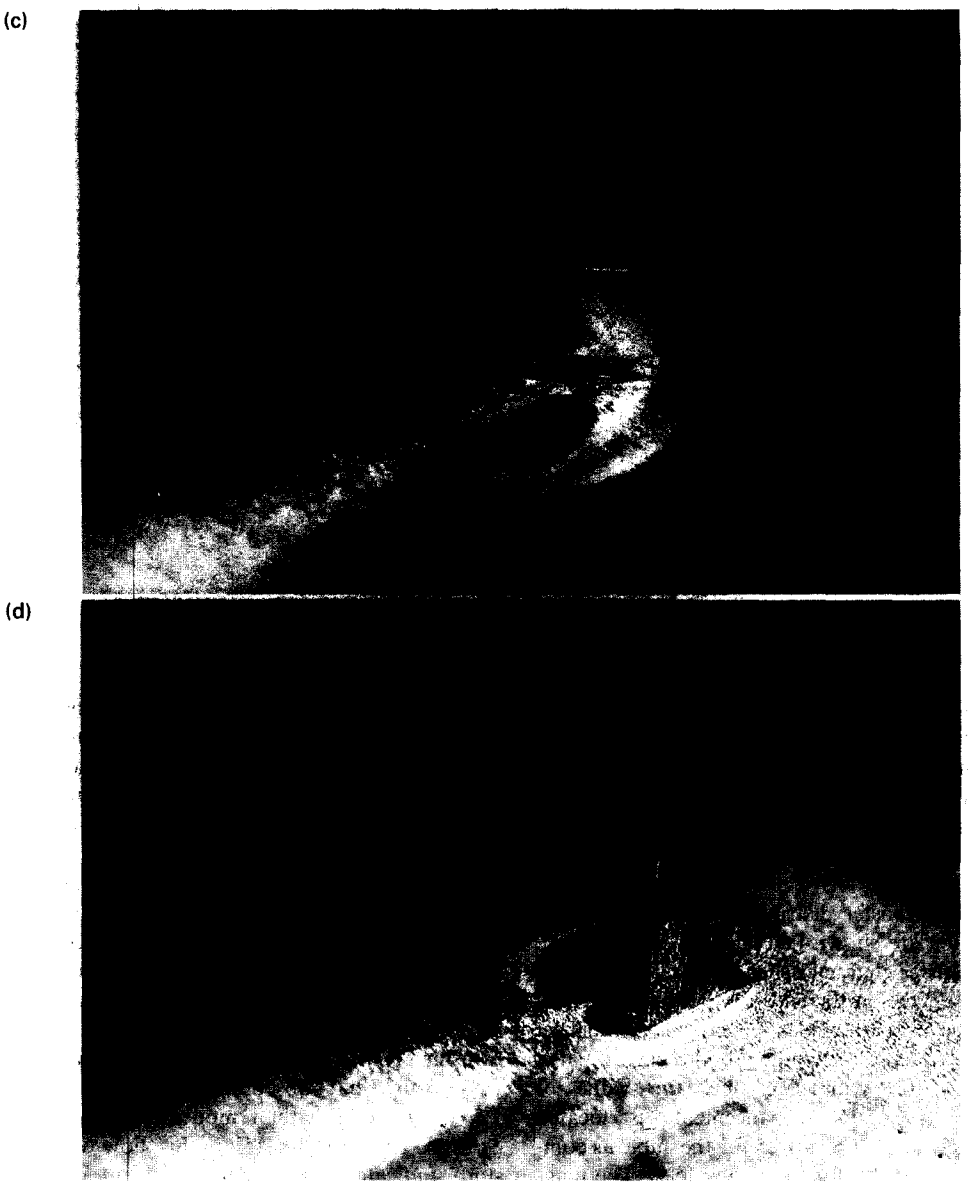

Fig. 4—*continued.*

lower with a thicker boundary layer, i.e. hydraulically smoother. This, in turn, induces lower heat or mass transfer.

Streakline patterns, shown in Fig. 4(a), observed on the wall support the aforementioned mass transfer characteristics. Traces of the primary and secondary horseshoe vortices wrapping around the base of the cylinder are evident. A dark line just ahead of the cylinder marks the boundary layer separation signifying the formation of the secondary vortex. The primary vortex initiates at the upstream most boundary of the domain influenced by the cylinder. The low pressure in the near-wake region behind the cylinder entrains both horseshoe vortices towards the centerline ($Z/D = 0$). Also seen in the region are the two lobular structures, observed as two spots of dark (graphite) flow accumulation. These lobes are characterized by vigorous motion and rotate in opposite directions with respect to one another. A similar flow structure, often termed the arch-shaped or inverted "U" vortex, has been visualised for flow over a cubical body [5, 9]. In fact, this vortex exists virtually for all the geometries investigated in the present study.

Further downstream, the shear layer separated atop the cylinder tends to dominate the core of the wake and impedes the inward movement of the horseshoe vortices. Turbulent mixing in this region is stronger along the spanwise direction than in the streamwise direction [19]. Overall, a "necklace" shaped flow pattern results, as shown in the figure. The shear layer eventually reattaches to the endwall, resulting in a mass transfer peak near the region $X/D \approx 2.0$. This is in very favorable agreement with the results reported by Mantle [15] and Goldstein *et al.* [2]. At re-

(e)

Fig. 4—*continued.*

attachment, part of the flow is diverted backwards towards the cylinder while the remaining fluid proceeds downstream. While such a dynamic effect cannot be captured by a still photo, it is vividly observed during the actual test.

Cube

Local mass transfer distributions around a wall-mounted cube are shown in Fig. 3(b). As expected, the mass transfer characteristics conform well to the streakline patterns on the endwall given in Fig. 4(b). The influence of a cubical element extends the farthest upstream of all the protruding bodies investigated here. Along the symmetric line, the value of $St/St_0 = 1.5$ (i.e. 50% enhancement) is located approximately at $X/D \approx -1.25$ for the cube, as compared to $X/D \approx -1.0$ for other obstacles. The magnitude of mass transfer keeps increasing toward the cube front and reaches a maximum, $St/St_0 \approx 2.0$, at $X/D = -1.0$ followed by a sharp rise, $St/St_0 \approx 3.0$, just ahead of the cube. According to a recent flow visualization [10], such highly elevated transfer coefficient near the cube front corner appears to be induced by a strong secondary vortex embedded underneath the primary horseshoe vortex. In fact, the cubical element has the highest level of enhancement upstream of the body among all five geometries examined.

Very high mass transfer ($St/St_0 \approx 3.0$) also prevails near the upstream section of the cube sidewalls. In an earlier study of mass transfer from the surface of a wall-mounted cube, Chyu and Natarajan [9] reported an unusually high heat transfer near such a corner junction. Low-frequency, periodic burstings were observed from the oil streaks accumulated in the region. This unsteady phenomenon is considered responsible for the elevated heat or mass transfer. The photo shown in Fig. 4(b) displays the dark graphite–oil mixture accumulated in the corner prior to a burst. This flow feature marks one of the most distinct characteristics for flow around a wall-mounted cube.

The "necklace" shaped streakline formation, seen earlier around a cylinder, is less conspicuous with the cube. This is due to its sharp-edged geometry and flat-frontal configuration. As a result, the domain of influence extends to $|Z_S/D| \approx 1.2$, about 20% greater than the cylinder. The region behind the cube is dominated by an arch-shaped vortex which promotes active mixing and results in relatively uniform and low heat transfer coefficients [9]. The effect of reattachment, while somewhat obscure, prevails in the region $1.5 \leqslant X/D \leqslant 2.5$ with a moderate enhancement at $St/St_0 \approx 1.8$. Mantle [15] in his flow visualization study indicated that the reattachment with a cube exists near $X/D = 2.5$ which is slightly further downstream compared to the cylinder ($X/D = 2.25$). Actual location of the flow reattachment as assessed by the bright region on the oil-covered endwall, shown in Fig. 4(b), in fact, agrees very favorably with Mantle's observation. This implies that location of the maximum transfer coefficient does not coincide exactly with that of the flow reattachment.

Diamond

Figure 3(c) shows the local St/St_0 characteristics around a wall-mounted diamond. Geometrically, a diamond shape is essentially a cube rotated 45° sideways relative to the direction of mainstream. Note that this rotation results in 40% more physical extension in both streamwise and spanwise directions in comparison to the cube. However, based on the present data, this increase in span does not bear any effect on furthering the influence upstream of the obstacle. Compared to a cubical element, not only is the domain

extended upstream smaller, but also the magnitudes of the transfer coefficients are lower. The wedge-shaped leading edge apparently tempers the extent of the flow separation and the strength of the horseshoe vortices. In addition, the feature of unsteady bursting near the upstream corner of the cube sidewall is not witnessed with the diamond. Chyu and Natarajan [10] have recently reported that the bursting phenomenon ceases if the cube orientation is 10° or more. With all these factors combined, magnitudes of the transfer coefficient in the region immediately adjacent to the two wedged, frontal walls are much smaller than their counterparts in a cube.

The wedge-shaped configuration of the frontal surface results in the largest lateral wake—spread amongst all the test geometries. The domain of influence is approximately $|Z_S/D| \approx 1.7$. In the region just behind the diamond, the influence of the arch-shaped vortex is significant. The arch-shaped vortex bridges both leeward surfaces, producing low mass transfer coefficients near the locations where the arch columns encounter the endwall ($St/St_0 \approx 1.25$). Further downstream, the value of St/St_0 recovers to reach a maximum, $St/St_0 \approx 2.4$, at $X/D \approx 2.5$. Not only is this the farthest location of reattachment-induced enhancement downstream to the obstacle, but also it has the highest value of maximum St/St_0 among all cases studied here. The key factor responsible for this phenomenon is a special flow feature atop the diamond. It is dominated by a pair of highly turbulent, delta-wing vortices as opposed to the commonly observed, recirculating bubble over a cube top-wall. As evidenced in a recent study by Chyu and Natarajan [10], these vortices substantially elevate the surface heat transfer underneath their tracks. It is expected that such influence persists further downstream as the shear layer reattaches to the endwall. While no information concerning the scalar transport around a wall-mounted diamond is available in the literature, results from the present study agree very favorably with those focusing exclusively on the momentum transport around a diamond-shaped obstacle [12, 15].

Pyramid

The results pertaining to a pyramid protrusion are shown in Figs. 3(d) and 4(d). The pyramidal geometry is characterized by a square base and four triangular faces culminating in a common vertex. In terms of the distribution in St/St_0, the pyramid shows a strong similarity to the cube where the influence upstream to the obstacle is significant. However, the domain of influence is much smaller, at about $|Z_S/D| \approx 0.8$. This is undoubtedly related to its tapering geometry and smaller frontal cross-sectional area. Another feature similar to the cube is that the flow near the lower upstream corner of the pyramid sides also shows an unsteady bursting phenomenon. The bursts appear to be more localized and centered around the spots with accumulated flow as shown in Fig. 4(d). Effects of these unsteady features on the local mass or heat transfer are clearly visible in Fig. 3(d), as two lobes of high magnitude of transfer coefficient ($St/St_0 \geqslant 2.0$) exist on either side of the element.

Largely because of its tapered shape, the pyramid permits a great deal of the high momentum oncoming flow to penetrate into the wake region. This strongly affects the lateral spread of the wake and reduces the spanwise extent of influence by the pyramid. As a result, the "necklace" shape is very apparent in the endwall streakline photograph, shown in Fig. 4(d). The other major effect is seen in the size of the inverted "U" vortex behind the pyramid, which stands greatly reduced. In addition, the vortex bears a vertical tilt and literally leans towards the back of the pyramid. Similar behavior has been observed around a wall-mounted cone by Okamoto *et al.* [19]. Compared to the flow behind a cube, this vortex produces higher rotational velocities and increased disturbances in the wake. This is partly responsible for the sharp recovery in mass transfer coefficient just behind the element. The highest enhancement in the wake region, $St/St_0 \approx 2.2$, occurs near $X/D \approx 1.0$, which is the shortest distance among all the geometries studied. However, one should note that its actual "trailing edge" of the "top wall", where the separated shear layer initiates, is located more upstream than that of other obstacles.

Hemisphere

Figure 3(e) shows the local St/St_0 distributions on a wall-mounted hemisphere. The flow around this geometry exhibits qualities resembling both that of a cylinder and a pyramid. The circular profile near the leading edge dictates the structure and strength of the horseshoe system. Downstream, the flowfield is dominated by the tapering cross-section which is similar to that of a pyramid, but without any sharp edges. This is apparently responsible for a narrow wake-spread, a "necklace" streakline pattern, and a short reattachment distance. The maximum value of St/St_0 (≈ 2.0) occurs at $X/D \approx 1.3$. The reattachment length is the second shortest, next only to the pyramid. However, its domain of influence is the smallest in size, but comparable to that of the pyramid, $|Z_S/D| \approx 0.7$. Savory and Toy [13, 14] have experimentally examined the influence of the approaching boundary layer on the flow characteristics around a hemisphere attached to the floor of a water tunnel. The reattachment based on their observation is $X/D = 2.5$ for a thin boundary layer and 1.5 for a thick boundary layer. The latter result agrees favorably with the present finding.

Comparison and average results

Table 1 lists some important results which include the reattachment length (X_R/D), the magnitude of maximum enhancement (St_m/St_0), and the span of the domain of influence (Z_S/D). Although some of the information listed in the table has been brought up in earlier discussion, the tabulated data provides a direct

Table 1. Features of flow and heat transfer around three-dimensional protrusions.

Geometry	δ/D	X_F/D Present	X_F/D Reference	X_R/D Present	X_R/D Reference	Z_S/D	$[St_m/St_o]$	$[St/St_o]_m$ Domain $-1.4 \leqslant x/D \leqslant 3.2$ $\lvert z/D\rvert \leqslant Zs/D$
Cylinder		−1.2		1.9	1.8 [15]	1.0	2.2	1.51
Cube		−1.4	−1.4 [6, 19]	1.9	2.0 [15]	1.2	1.8	1.54
					2.1 [6]			
Diamond		−1.3	−1.4 [19]	2.5	3.0 [15]	1.7	2.4	1.53
	1.06				1.9 [19]			
Pyramid		−1.1		1.0		0.8	2.2	1.50
Hemisphere		−1.0		1.3		0.7	2.0	1.35
Cylinder		−1.1		1.9				
Cube	0.33	−1.0	−1.1 [19]	1.9	1.9 [19]			
Diamond				2.3	2.3 [19]			

comparison between the different geometries. It is clear that the diamond has the strongest reattachment-induced enhancement with the widest spread in the wake region. In addition, its reattachment length is also the longest. On the other hand, the cube has the lowest value of enhancement downstream to the obstacle, about 25% lower than the diamond. However, it has very substantial enhancement just upstream to the element. The hemisphere has the shortest reattachment length, about 40% of the diamond case. In terms of the wake span, measured by the boundary of at least 25% enhancement, the hemisphere is the narrowest which is nearly 60% narrower than the diamond. An interesting observation is that the cylinder is positioned in the intermediate range virtually for all the parameters listed in the table.

To assess the relative enhancement potentials between the different elements, it is worthwhile to define an effective area-averaged mass transfer parameter $(St/St_0)_m$ over the domain of influence for the element–wall combination. As listed in Table 1, the values of $(St/St_0)_m$ for cylinder, cube, diamond and pyramid are very comparable, ranging from 1.50 to 1.54. Since the domain of influence varies between elements, the actual area for which these numbers are calculated are different for each element. The hemisphere–wall combination enhances about 10 to 15% lower mass transfer than that of other elements.

The knowledge of the extent of transverse flow disturbance is valuable in providing guidelines for the design of a heat exchanger surface mounted with an array of elements. For a rough surface to be effective, it is imperative that the influence of flow disturbance must be perceived at all locations on the heat transfer surface. Hence, neighboring elements can be positioned such that the region in between them is completely affected by the disturbed flow. This can be attained with inter-element spacings equal to approximately twice its lateral spread. For example, for the cylinder, the spanwise domain of influence at the origin is $|Z_S/D| = 1.0$. Using this, an inter-element spacing for a cylinder array can be suggested to be around 2.0. An interesting observation is that the optimal inter-cylinder spacing currently recommended for pin–fin cylinder arrays, used in blade cooling, is roughly 2.0–2.5, which is fairly close to the value presently suggested. With this approach, it can be speculated that for a given test surface size, the number of elements required to achieve effective heat transfer enhancement can be minimized using diamond geometry. Likewise, because of their smallest lateral influences on the flowfield, a test surface mounted with pyramids or hemispheres will require the largest number of elements. Such information will lead to a direct estimate of the actual surface area for heat transfer. Combined with the heat transfer coefficient data revealed in the present study, the total amount of heat transfer from a roughened surface can be assessed.

CONCLUSIONS

Local heat transfer from a flat surface mounted with a single roughness element is examined at a flow Reynolds number of 1.7×10^4. A mass transfer system based on the naphthalene sublimation technique is used to obtain heat transfer information and is demonstrated to be highly suitable for investigating situations involving steep thermal gradients. Heat transfer enhancement induced by five different basic roughness geometries (cylinder, cube, diamond, pyramid, hemisphere), with identical height or diameter, are comparatively examined. For all the cases studied, the convective transport is largely dominated by the formation of the upstream horseshoe vortex system as well as the wake vortices downstream to the element. Diamond induces the longest reattachment length downstream, followed by cube, cylinder, pyramid and hemisphere.

An effective area-averaged mass transfer parameter $(St/St_0)_m$ for the element–wall combination is evaluated, and these are comparable for cylinder, cube, diamond and pyramid, and about 15% higher than that of hemisphere. Based on the extent of transverse flow disturbance, inter-element spacings are recommended for array configurations. It is expected

that, for a given surface, the least number of elements required to achieve effective heat transfer enhancement will be on a test surface of diamond geometry. On the contrary, a pyramid or hemisphere arrangement will require the largest number of elements.

REFERENCES

1. D. F. Dipprey and R. H. Sabersky, Heat and momentum transfer in smooth and rough tubes at various Prandtl numbers, *Int. J. Heat Mass Transfer* **6,** 329–353 (1963).
2. R. J. Goldstein, M. K. Chyu and R. C. Hain, Measurement of local mass transfer in the region of the base of a protruding cylinder with a computer-controlled data acquisition system, *Int. J. Heat Mass Transfer* **28,** 977–985 (1985).
3. M. K. Chyu and R. J. Goldstein, Influence of cylindrical elements on local mass transfer from a flat plate, *Int. J. Heat Mass Transfer* **34,** 2175–2186 (1991).
4. E. M. Fisher and P. A. Eibeck, The influence of a horseshoe vortex on local convective mass transfer, *J. Heat Transfer* **112,** 329–335 (1990).
5. J. C. R. Hunt, C. J. Abell, J. A. Peterka and H. G. C. Woo, Kinematical studies of flows around free or surface-mounted obstacles; applying topology to flow visualization, *J. Fluid Mech.* **86,** 179–200 (1978).
6. R. Martinuzzi, C. Tropea and J. Volkert, Observations on flow over prismatic obstacles in a fully developed channel flow, *Proceedings of the UTAM Symposium on Bluff Body Wakes, Dynamics and Instabilities*, Springer, New York, pp. 201–204 (1992).
7. H. G. C. Woo, J. A. Peterka and J. E. Cermak, Wind-tunnel measurements in the wakes of structures, NASA CR-2806 (1977).
8. H. Werner and H. Wengle, Large-eddy simulation of turbulent flow over and around a cube in a plate channel, *Turbulent Shear Flows* **8,** 155–168 (1993).
9. M. K. Chyu and V. Natarajan, Local heat/mass transfer distributions on surface of a wall-mounted cube, *J. Heat Transfer* **113,** 851–857 (1991).
10. M. K. Chyu and V. Natarajan, Effect of flow angle-of-attach on the local heat/mass transfer distributions from a wall-mounted cube, *J. Heat Transfer* **116,** 552–560 (1994).
11. J. Olsen, B. W. Webb and M. Queiroz, Local three-dimensional heat transfer from a heated cube, ASME Winter Annual Meeting, San Francisco (1989).
12. Y. Ogawa, S. Oikawa and K. Uehara, Field and wind tunnel study of the flow and diffusion around a model cube—I. Flow measurements, *Atmospheric Environment* **17**(6), pp. 245–261 (1983).
13. E. Savory and N. Toy, The flow regime in the turbulent near wake of a hemisphere, *Exp. Fluids* **4,** 181–188 (1986).
14. E. Savory and N. Toy, The separated shear layers associated with hemispherical bodies in turbulent boundary layers, *J. Wind Engng Ind. Aerodyn.* **28,** 291–300 (1988).
15. P. L. Mantle, A new type of roughened heat transfer surface selected by flow visualization techniques, *Proceedings of the 3rd International Heat Transfer Conference*, pp. 45–55 (1966).
16. E. R. G. Eckert, Analogies to heat transfer processes *Measurements in Heat Transfer* (Edited by E. R. G. Eckert and R. J. Goldstein). Hemisphere, Washington D.C. (1976).
17. D. Ambrose, I. J. Lawrenson and C. H. S. Sparke, The vapor pressure of naphthalene, *J. Chem. Thermodyn.* **7,** 1173–1176 (1975).
18. F. P. Incropera and D. P. Dewitt, *Fundamentals of Heat and Mass Transfer* (3rd Edn), John Wiley, New York (1990).
19. Tetsushi Okamoto, Miki Yagita and Shin-ichi Kataoka, Flow past a cone placed on a flat plate, *Bull. JSME* **20,** 329–336 (1977).
20. P. H. Chen, Measurement of local mass transfer from a gas turbine blade, Ph.D Thesis, University of Minnesota (1988).
21. M. K. Chyu and V. Natarajan and D. E. Metzger, Heat/mass transfer from pin–fin arrays with perpendicular flow entry. *Fundamentals and Applied Heat Transfer for Gas Turbine Engines*, ASME HTD-226, 31–39. ASME, New York (1992).
22. R. J. Goldstein, S. Y. Yoo, M. K. Chung, Convective mass transfer from a square cylinder and its base plateau, *Int. J. Heat Mass Transfer* **33,** 9–18 (1990).